Optimisation of the process of X-ray tomography applied to the detection of defects in composites materials

Cyril Uhry, François Guillet, Philippe Duvauchelle, Valérie Kaftandjian

Optimisation of the process of X-ray tomography applied to the detection of defects in composites materials

Cyril UHRY[1], François GUILLET[1], Philippe DUVAUCHELLE[2], Valérie KAFTANDJIAN[2]
[1] CEA, DAM, Le Ripault F-37260 MONTS, France ; Phone : +33 247345753 ; e-mail : cyril.uhry@cea.fr, françois.guillet@cea.fr
[2] Laboratoire Vibrations et Acoustique, INSA de Lyon ; Villeurbanne, France ; e-mail : philippe.duvauchelle@insa-lyon.fr, valerie.kaftandjian@insa-lyon.fr

Abstract: Computed tomography (CT) is a relevant nondestructive inspection method for composite material. However, X-ray attenuation contrast difference between fibers and matrix can be low, which makes identification of defects difficult. Optimization of the tomographic process has then to be considered, such as studying the acquisition parameters and phenomena that decrease the contrast. Simulation of the CT method is considered in order to optimize contrast between fibers and matrix. Simulation allows to study phenomena independently to the others. Phantom was built in order to check the accuracy of the computation. Even though results show discrepancies between computation and experimental measurements, these discrepancies have been found to be due to an experimental artefact. When corrected, simulation fits very well with experimental results and this procedure allows to seek an optimal setup for composite material inspection.

Keywords: computed tomography, X-ray detectors and sources, defect detection, scattering, simulation, X-ray imaging, non-destructive testing, virtual X-ray imaging

1 Introduction

Because of their outstanding properties [1], carbon fiber-reinforced polymers (CFRP) are the favorite candidate for lightweight thermo-structural applications, like in the aerospace industry. In this study, we will focus on carbon fiber reinforcement composites materials with epoxy resin matrix such as hydrogen reservoirs. These reservoirs are composed of filament of carbon fibers impregnated with epoxy resin. The architecture of the composite material is obtained by filament winding around a cylindrical polyamide liner. Architecture plays an important part for obtaining good properties.
However, defects in composites cannot be avoided and occur either during the manufacturing process, or during usage (impact, fatigue). Depending on their nature and size, they can decrease the thermo-mechanical properties of the material. Defects can be porosities in the resin, delamination between woven tissue, or cracks in fibers [2] [3].
Thus, accurate non-destructive inspections are mandatory, such as X-ray computed tomography. CT provides three-dimensional images of internal structure of material, allowing detection of defects, as porosities or delamination [4] [5].
Distinction between porosities and composite material (carbon fiber or epoxy resin) in CFRP is possible due to the relative high density contrast and chemical composition difference between porosities (air or trapped gas) and carbon or epoxy resin. The difference of linear attenuation coefficient is consequently enough for observing this type of defects. However, the distinction between carbon reinforcement and epoxy resin to identify architecture defects is much more complex. A typical epoxide polymer is composed of 76 wt% (weight percentage) of carbon, 17 wt% of oxygen and 7 wt% of hydrogen. The densities of epoxy polymer and carbon fiber are close (typically 1.8 for carbon fiber and 1.2 for epoxy resin). This leads to a low attenuation coefficient difference at voltages required for inspecting objects and consequently to a low contrast in CT scan.

X-ray computed tomography allows observation of the internal structure of hydrogen reservoir. Figure 1 display a photo of a hydrogen reservoir (a), a slice perpendicularly to its revolution axis (b) and a cylindrical slice along the blue line in (b). Identification of the filament orientation is difficult. However, a high proportion of porosities make their identification easier.

As the contrast difference between epoxy resin and fiber is weak, optimization of the tomographic process should be considered, beginning with experimental parameters such as voltage. Phenomena decreasing contrast in CT scans such as scattered radiation has also to be studied.
A usual approach to carry out optimization is computer modelling and simulation. It allows to study independently the influences of the phenomena [6] [7], or the optimal set-up parameters [8] [9], with the advantage of reducing the experimental acquisition as much as possible.
In this study, computation of projections is carried out using the deterministic software VXI (Virtual X-ray Imaging) [10]. It allows to compute a set of projection that is reconstructed using the software DigiCT (Digisens).
Because of the weak contrast between carbon and epoxy resin, it is very important that the computation are as much accurate as possible. In order to check the accuracy of results, a simple phantom object is considered. Experimental projections and CT scans of this object are compared to the one computed using VXI and the differences are discussed.

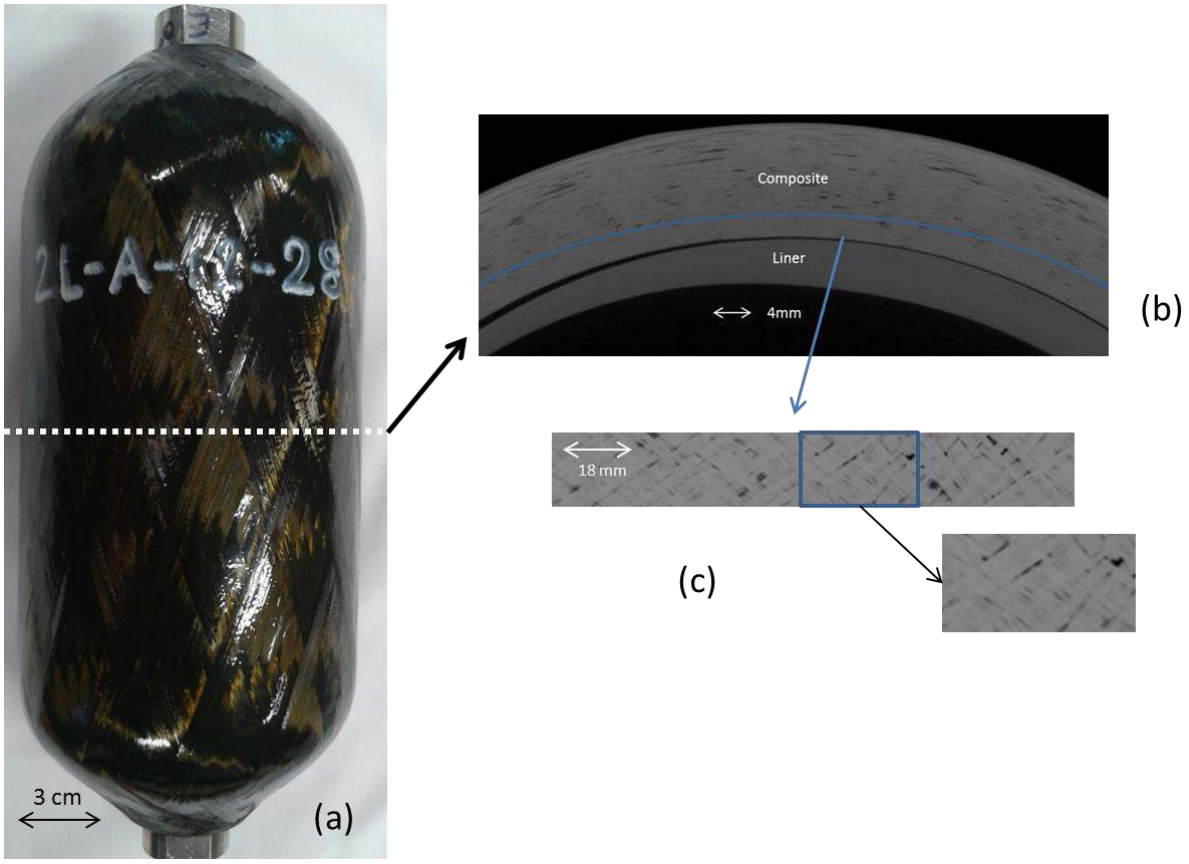

Figure 1: a) photo of a hydrogen reservoir, b) CT slice perpendicularly to its revolution axis c) cylindrical slice along the blue line in (b) displaying tow architecture in reservoir

2 Material and methods

2.1 Phantom object

The geometry, size and chemical composition of the phantom object were chosen to be close to the characteristics of hydrogen reservoirs, particularly the filament winding around the liner. The object proposed here is a hollow cylinder consisting in a succession of hollow cylinders of pure graphite and epoxy resin corresponding successively to the filament winding of carbon fiber and epoxide polymer (Figure 2) . K10 graphite and RSF 816 epoxy resin were chosen due to availability and good representativeness of actual materials.
The phantom is approximately 8 cm high, with a diameter of 10 cm. It is composed of four graphite cylinders and three RSF 816 epoxy cylinders, each layer being 2 mm thick.
A chemical analysis was performed on both materials so as to compute the most accurate linear attenuation coefficient possible. Analysis shows that the graphite is composed of 93 wt% of carbon, with impurities (1.1 wt% silicon and 1.1 wt% sulphur). This heavier atoms account for a significant part of linear attenuation coefficient. A precise knowledge of chemical composition is therefore very important. The RSF 816 epoxy resin is relatively close to epoxy resin, 71 wt% of carbon, 17 wt% oxygen and 8 wt% of hydrogen and a low percentage of heavy weight atoms (chlorine 0.6 wt%).
So as to validate the chemistry of materials homogeneous samples of graphite and RSF 816 epoxy resin were exposed to X-rays. Computed and experimental projections were compared for different high voltages. The difference between measured and computed X-ray intensity after attenuation for both materials is less than 2 % for a range of voltage between 60 kV and 200 kV.

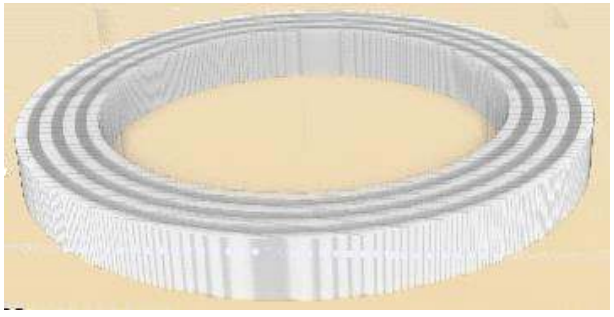

Figure 2: the phantom composed of K10 graphite and RSF 816 epoxy resin hollow cylinders

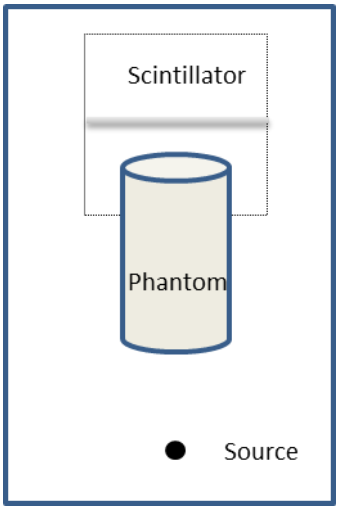

Figure 3: schema of the montage acquisition

2.2 Projection computation

Virtual X-ray Imaging (VXI) is a deterministic simulation code allowing the simulation of X-Ray radiography of three-dimensional objects. This code is based on ray-tracing technique and the attenuation law of photons passing through an object. The description of the principle

of the simulation can be found in [10] and [11]
VXI allows computation of the projections of the primary radiation, defined as photons that do not undergo interaction before reaching the detector. The computation of the scattered radiation is carried out separately. Only the first-order scattering is considered, higher orders of interaction are neglected.

Projections are computed as follows:

1. The primary radiation I_p and scattered projection I_s: primary and scattered radiations are computed on the central line of the cylinder (on the central line of the Figure 3). Given the symmetry of the cylinder, projection is considered to consist of copies of this line along the vertical axis. Thus, the cylinder is considered to be infinite along the revolution axis.
2. Computation of the images without any object: I_{white}.
3. Normalization of I_p and I_s with I_{white}: $I_{p,s_{normalized}} = c\frac{I_{p,s}}{I_{white}}$. I_p and I_s are computed by calculating the energy deposited in the scintillator, in MeV. Normalization with I_{white} allows obtaining projections free of unit, as obtained experimentally. As the format of the image is 16 bits, the constant c is arbitrarily fixed to $c = 30000$, corresponding approximately to $2^{16}/_{2}$.
4. The final projection image $T_{normalized}$: $T_{normalized} = I_{p_{normalized}} + I_{s_{normalized}}$.

2.3 Measurement system

The set-up consists in a X-Tek Micro 225kV X-ray tube with a reflective tungsten target. The detector is a 4000x4000 pixels Photonic Science Image Star Large Area, with approximately 100 microns square pixels. The scintillator is composed of a 300µm columnar CsI (Caesium Iodine) layer deposited on a 1 mm thick aluminium substrate. Visible photons emitted by the scintillator are reflected on a 45° mirror and focused on a CCD camera by a coupling lens. The CCD area is 37x37mm with 9 microns square pixels. Images present artefacts due to the detector such as vignetting artefact (intensity is higher in the centre of the image than in the corner) barrelling distortion and dark current of the photodiodes. Images are corrected from gain and offset using equation 1.

$$I_{normalized} = c\frac{I_{raw} - I_{black}}{I_{white} - I_{black}} \quad (1)$$

With I_{raw} being the as-measured image, I_{black} is an image without X-ray exposition, I_{white} an image without object, $c = 30000$ as previously described.

Objects considered in the study are hollow cylinders. In the simulation, their axis of revolution corresponds to the axis of rotation of the tomographic acquisition. Consequently, only one projection $T_{normalized}$ is computed with XVI, and then duplicated as much as required. Noise can be added to the simulated projection during duplication, but this is not in the scope of this article.
Whether projections are computed or experimental, CT reconstructions are performed using

DigiCT (DigiSens software version 3.2) using FDK algorithm and Hanning filter.

3 Results

3.1 Experimental parameters:

Measurement of the phantom objet is performed for a 90 kV accelerating voltage, with an exposure of 8.9 s and an intensity current of 550 µA. The source-object distance is 300 mm and the object-detector distance is 620 mm. A set of 3600 projections are measured along 360°. The reconstruction volume corresponds to the central part of the phantoms. Its size is 106.6 mm x 106.6 mm x30 mm, with a 100 µm voxel size.

3.2 Projections

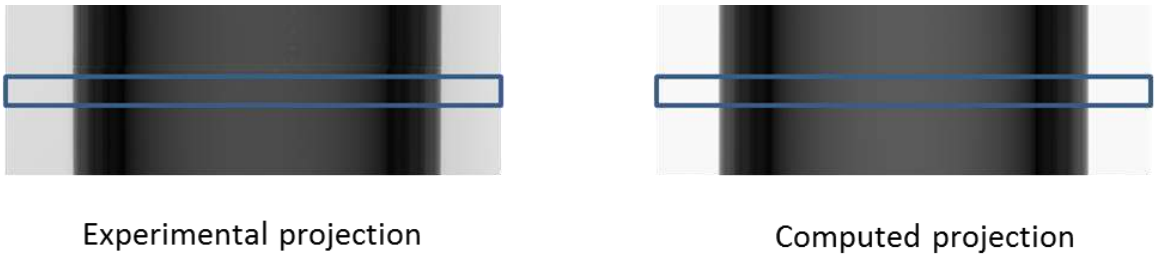

Figure 4: comparison of experimental and computed projections

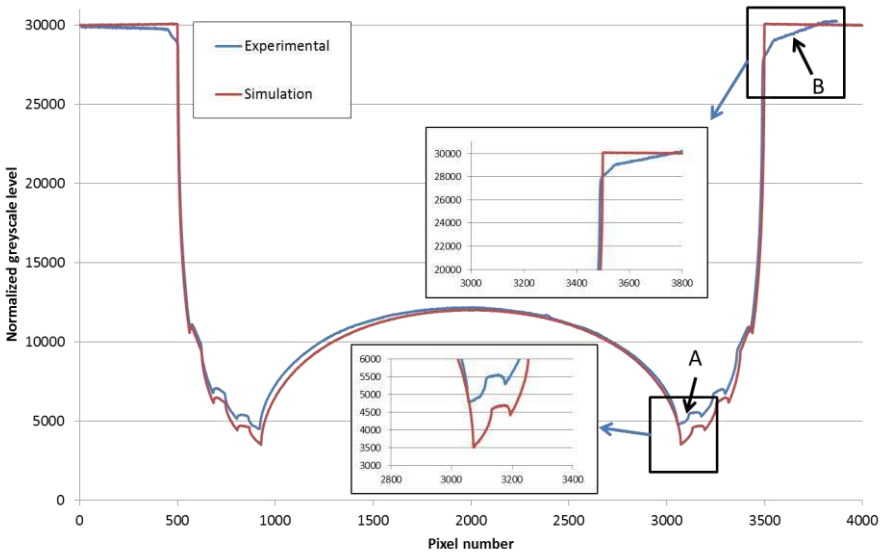

Figure 5: comparison of experimental and simulated projections profile

Computed and experimental projections are compared in Figure 4. Figure 5 presents the greyscale profile along the region of interest in the Figure 4.
Computed grey level is close to experimental grey level. However, some discrepancies can be

noticed. First, in the region of the highest attenuation (labeled A in the Figure 5), computed profile overestimates grey level by 25%. Second, the right and left maximum value of experimental grey level should be symmetric. However, the right maximum is 6% lower than the left maximum in the experimental projection and is lower than the expected 30.000 value (label B in the Figure 5).
Comparison between computation and experiment was performed for other voltages (140kV, 160kV, 200kV): the same differences were observed.

3.3 Computed tomography

Figure 6 shows a planar slice of the volume, perpendicular to the axis of revolution of the cylinders, for both experimental and computed reconstructions. Bright layers correspond to graphite cylinders and dark cylinders to RSF 816 layer, as darker grey level corresponds to weaker values of linear attenuation coefficient.
Heterogeneities can be observed in the graphite layers (see arrows in Figure 7). Linear attenuation coefficient is higher in the border than in the center, which would correspond to higher graphite density in the border of the cylinders. Graphite cylinders were cut from blocks of graphite, a process which could account for higher densities close to the cutting zone.

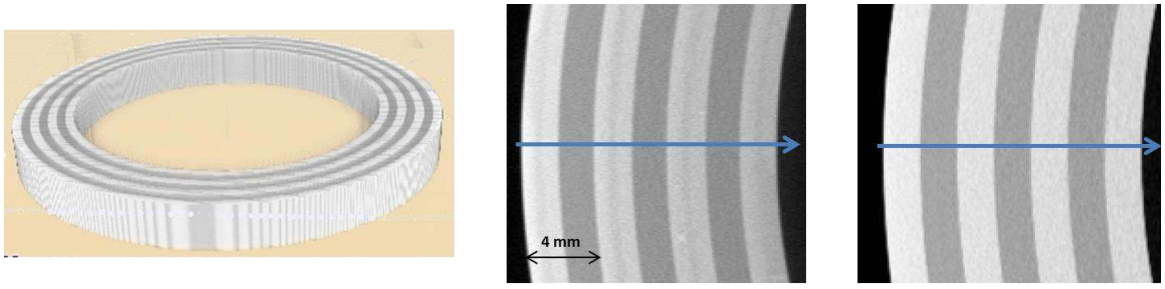

Figure 6: simulated and experimental simulation

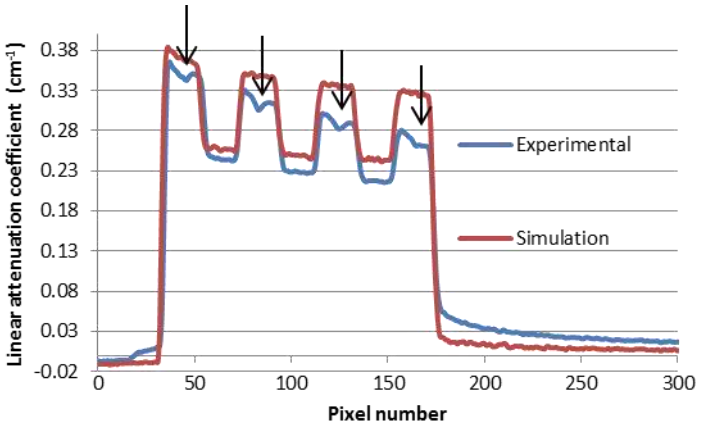

Figure 7: comparison of the reconstructed profile (mean over 50 lines)

Figure 7 presents the linear attenuation coefficient along the arrow shown on Figure 6. The line crosses successively graphite and RSF 816 layers, beginning with the external composite

layer on the left of the profile (Figure 7). As deeper layers are crossed, linear attenuation coefficient decreases. This is the well-known cupping effect due to the polychromatic nature of the beam.
The comparison of profiles shows that the computed linear attenuation coefficient is higher than the experimental linear attenuation coefficient. The overestimation increases as deeper layers are considered (relative difference of 5% for the external graphite layer and 15% for the internal graphite layer). This is consistent with projection comparison (Figure 5): computed attenuation is overestimated where the attenuation is maximal at the internal border of the object. This leads to a higher linear attenuation coefficient.

4 Discussion

A plausible hypothesis for the discrepancies between computation and experimentation is that the mirror in the camera backscatters X-rays towards the scintillator. X-rays photons that go through the scintillator without being absorbed are backscattered by the mirror (Figure 8). They are then absorbed and contribute to the projection.
The mirror is tilted 45° from the direction of the propagation of X-rays. It is closest to scintillator at the right side of the detector. Consequently, backscattered radiation is more important at the right side because of the higher solid angle per detector unit length.
Backscattered radiation was experimentally estimated using a lead panel in front of the scintillator covering its entire surface, except for a vertical band along z axis of 1.5 cm width, where X-rays can reach the scintillator. Backscattered radiation is then measured on each side of the band, behind the lead panel. Figure 9 display a profile along the y axis for the open band at the right side of the detector and left side of the detector. Scattered intensity is higher at the right side, as it is consistent with the hypothesis of backscattered radiation. The scattered intensity drop at the right of the detector (label A on Figure 9) can not be explained considering the mirror alone but can be due to the actual camera setup (e.g. mirror mounting).

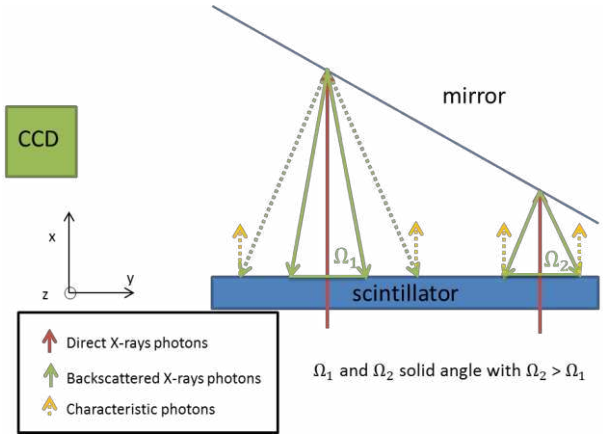

Figure 8: backscattering in the detector

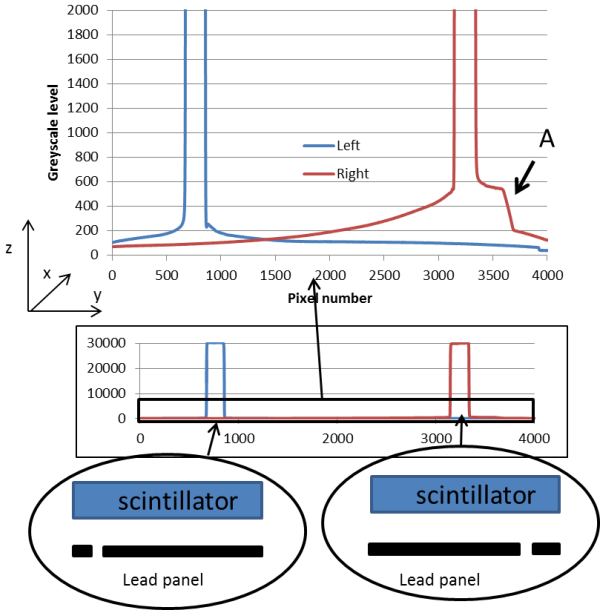

Figure 9: profile behind lead panel

In order to estimate backscattered radiation along the entire width of the detector,

measurements were carried out by translating the lead panel along y. Backscattered radiation profiles were considered on the central line of the projection along z for each position of the panels. These profiles allow computation along the central line of the backscattered radiation $I_{backscattered}$ of a measured projection $I_{measured}$.

$$I_{backscattered} = \alpha . I_{transmitted} \approx \alpha . I_{measured} \quad (2)$$

$I_{backscattered}$ is proportional to $I_{transmitted}$, defined as the intensity corresponding to X-ray photons that are not backscattered. $I_{backscattered}$ is considered to be approximately proportional to $I_{measured}$. Several approximations are made. First, the backscattered profile is not measured for a unique pixel, but for a band along z with a width of 1.5 cm along y. This measurement integrates contribution from the whole 1.5 cm width as well as the height of the band. This second point is however not a problem due to the vertical symmetry of the objects considered in this study.
Border effects are also neglected as backscattering is less important at the top and bottom of the image.
Figure 10 displays projection profiles of phantom and white images compared to computed backscattered intensity. As expected, backscattered radiation is higher at the right side of the projection. It is also higher in the white image than in the phantom projection, since it is proportional to intensity reaching scintillator in the first place.

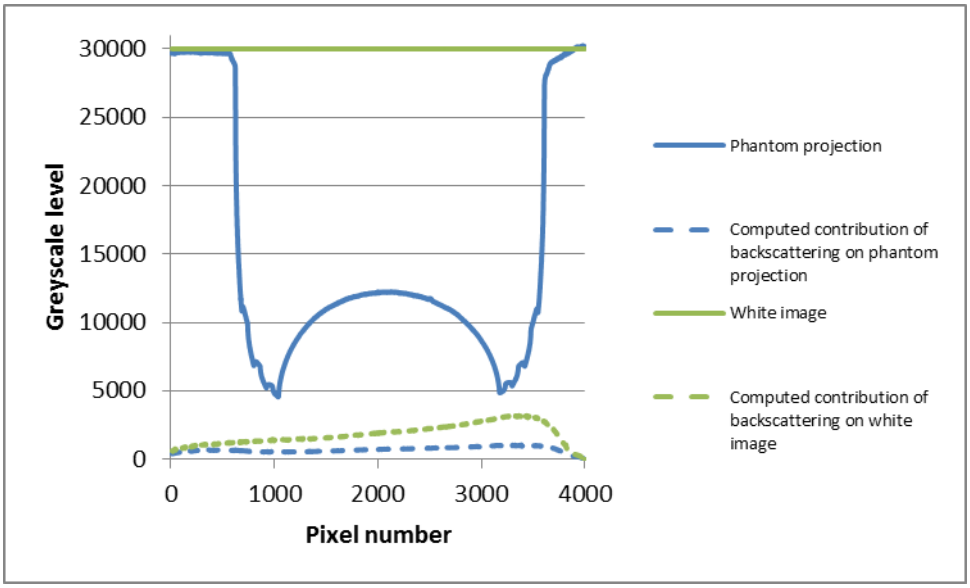

Figure 10: phantom projection and white image and the respective computed contribution of backscattering to experimental image

Computed backscattered signal (Equation 2) has been added to computed projections, and were compared to experimental ones (Figure 11). Grey level at the right of the image is now lower than 30000, close to the experimental profile (label B in Figure 11).
Grey level of the highest attenuation region (label A in Figure 11) is increased and is also closer to experimental values.

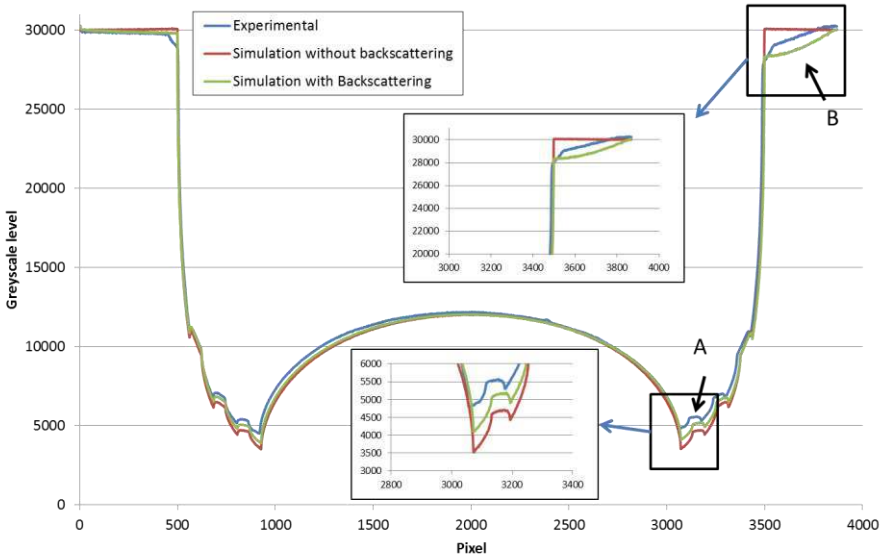

Figure 11: comparison of experimental projections and simulation with backscattering

Computed tomographic reconstruction was performed using projections corrected with the backscattered radiation (Figure 12). The linear attenuation coefficient is much closer to experimental values. The cupping effect is also increased and matches the experimental one.

This coarse computation of backscattering allows to get closer to experimental projections and CT scans. However, it is not fully accurate and further work is necessary.

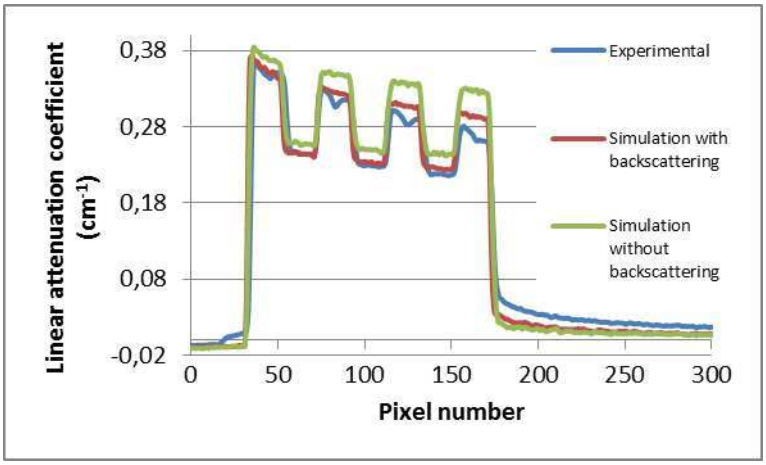

Figure 12: comparison of the reconstructed profile with backscattered radiation

5 Conclusion

In order to optimize the tomographic process, simulation is a relevant tool as it allows to study each different phenomenon independently to the others. However, it has to be checked

against experiment. To this end, a phantom was built. The materials of the phantom were chosen for best representativeness of carbon fibers and epoxy resin especially with respects to chemistry. Heavy impurities can change significantly the linear attenuation coefficient, and greatly influence contrast between carbon fiber and epoxy resin which is weak. Comparisons of computed and both measured projections and CT scans were performed. Results reveal discrepancies that allowed to identify a backscattering phenomenon. Its computation allowed to better fit the experimental results, even with a rough estimation.

6 References

[1] S. Ozcan, J. Tezcan and P. Filip, "Microstructure and elastic properties of individual components of C/C composites," Carbon, vol. 47, no. 15, pp. 3403-3414, 2009.

[2] H. yan Zhu, D. hong Li, D. xing Zhang, B. chang Wu and Y. yong Chen, "Influence of voids on interlaminar shear strength of carbon/epoxy fabric laminates," Transactions of Nonferrous Metals Society of China, Vols. 19, Supplement 2, no. 0, pp. s470 - s475, 2009.

[3] A. Shigang, F. Daining, H. Rujie and P. Yongmao, "Effect of manufacturing defects on mechanical properties and failure features of 3D orthogonal woven C/C composites," Composites Part B: Engineering, vol. 71, no. 0, pp. 113-121, 2015.

[4] T. Centea and P. Hubert, "Measuring the impregnation of an out-of-autoclave prepreg by micro-CT," Composites Science and Technology, vol. 71, no. 5, pp. 593-599, 2011.

[5] P. J. Schilling, B. R. Karedla, A. K. Tatiparthi, M. A. Verges and P. D. Herrington, "X-ray computed microtomography of internal damage in fiber reinforced polymer matrix composites," Composites Science and Technology, vol. 65, no. 14, pp. 2071-2078, 2005.

[6] G. Jarry, S. Graham, D. Mosoley, D. Jaffray, J. Siewerdsen and F. Verhaegen, "Characterization of scattered radiation in kV CBCT images using Monte Carlo simulations," Medical Physics, vol. 33, no. 11, pp. 4320-4329, Nov 2006.

[7] P. Wils, J. M. Létang and J.-P. Bruandet, "Secondary radiations in CBCT: a simulation study," Journal of Electronic Imaging, vol. 21, no. 2, pp. 021113-1-021113-9, 2012.

[8] K. Tigkos, K. Bliznakova, A. Dermitzakis, N. Ducros, U. Hassler, Z. Kamarianakis, A. Osman, V. Rebuffel and M. Tartare, "Simulation study for optimization of X-ray inspection setup applied to SFRP aerostructures," in ICT Conference 2014, 2014.

[9] J. Hiller and L. M. Reindl, "A computer simulation platform for the estimation of measurement uncertainties in dimensional X-ray computed tomography," Measurement, vol. 45, no. 8, pp. 2166-2182, 2012.

[10] P. Duvauchelle, N. Freud, V. Kaftandjian and D. Babot, "A computer code to simulate X-ray imaging techniques," Nuclear Instruments and Methods in Physics Research Section B: Beam Interactions with Materials and Atoms, vol. 170, no. 1–2, pp. 245-258, 2000.

[11] N. Freud, P. Duvauchelle, S. Pistrui-Maximean, J.-M. Létang and D. Babot, "Deterministic simulation of first-order scattering in virtual X-ray imaging," Nuclear Instruments and Methods in Physics Research Section B: Beam Interactions with Materials and Atoms, vol. 222, no. 1–2, pp. 285-300, 2004.